JOURNAL OF AIRCRAFT
Vol. 43, No. 2, March–April 2006

Validation of Computations Around High-Lift Configurations by Structured- and Unstructured-Mesh

Mitsuhiro Murayama* and Kazuomi Yamamoto†
Japan Aerospace Exploration Agency, Tokyo 182-8522, Japan
and
Kunihiko Kobayashi‡
Ryoyu Systems Company, Ltd., Tokyo 108-0074, Japan

In this study, flow computations are performed on two-dimensional and three-dimensional high-lift configurations on multiblock structured and unstructured meshes. The objectives are to assess and improve the reliability in simulating the flow around such devices. First, two-dimensional computations on two-element and three-element airfoils are performed to investigate mesh dependency in detail. For unstructured meshes, this is carried out by using a mesh-refinement approach. The results show that sufficient mesh density away from the wing surface is required for accurate drag prediction because the flow has large circulation and wake. A mesh-refinement approach using entropy increment as the refinement indicator is also applied, and its effectiveness is validated. The method is effective in increasing the mesh points in the region of physical importance, such as wake, and the region where the numerical error is high. Three-dimensional computations on three-element trapezoidal wings with fuselage are also performed, and some modest grid studies are performed with structured meshes. Two configurations with full-span flap and part-span flap are used. Ways to improve the reliability of structured and unstructured meshes are discussed by comparing the results. The prediction of aerodynamic forces is quite reasonable even on the unstructured mesh at moderate settings of slat and flap, despite minor differences in local flow physics. However, it is also shown that the unstructured meshes should be further refined to resolve the wake near trailing edge, wing-tip vortices, and the flow separation at the juncture of the wing and body for more accurate prediction.

I. Introduction

FOR a successful design of an aircraft, the development of efficient high-lift devices is one of the important requirements. Performance of high-lift devices has a strong and direct impact on the operating cost of the aircraft. For a large commercial aircraft with twin jet engines, 1% improvement of the lift-to-drag ratio at takeoff allows a 2800-lb increase in payload, whereas 1.5% improvement of the maximum lift coefficients at landing allows a 6600-lb increase in payload.[1] From the point of view of jet engine noise, low drag at takeoff and landing is also desirable. Recent development in computational fluid dynamics (CFD), especially concerning the solution of compressible Reynolds-averaged Navier–Stokes equations, and optimization algorithm has led to high expectation in performance improvement.[2–4] Precise prediction of the aerodynamic forces is required for the design of a high-lift system.

However, CFD analysis for high-lift system still faces several difficulties. A commonly used high-lift device is a multi-element wing system, comprising slat, main, and flap elements. CFD mesh generation around the high-lift configuration is troublesome because of the complexity of the configuration and small gaps. In addition, the flow physics around a high-lift configuration is complicated as a result of boundary-layer transition, flow separation, reattachment, and interaction of wake and boundary layer. Insufficient resolution of such important phenomena can lead to significant error in aerodynamic forces. Even for two-dimensional computations, it is still difficult to predict the flow physics consistently. To develop an aerodynamic design system, problems associated with the mesh generation and accuracy of CFD for such a complicated flowfield have to be addressed.

Recently, efforts to validate and improve CFD have been made for high-lift systems.[5] In the EUROLIFT project,[6] development of aerodynamic analysis for a high-lift system on highly complicated three-dimensional full aircraft configurations has been intensively conducted in conjunction with experiments. In the NASA Langley 14×22-Foot Wind Tunnel and NASA Ames 12-Foot Pressure Wind Tunnel, a trapezoidal high-lift wing with body pod has been tested, and the experimental data are provided for validation and development of CFD methods for three-dimensional high-lift flows. Several computations have been conducted,[7] and wind-tunnel interferences have also been investigated.[8] The results indicated that it is necessary to model the wind tunnel in the computations to compare the local flow quantities with the wind-tunnel test data.

The model deploying the slat and flap generates considerable lift, which results in large wall-interference corrections.[8] To validate and develop the CFD methods, a detailed comparison of computational results from several CFD codes and mesh topologies is helpful. Multiblock structured mesh CFD has the advantage of low computational costs and high solution accuracy. However, it requires a large amount of time to generate. On the other hand, the unstructured mesh method has the capability to handle the complicated configurations associated with high-lift devices in a much shorter time. In addition, it is much easier to modify the mesh when the geometry changes as a result of optimization study or when adaptive mesh refinement is employed.[9,10] Therefore, it is hoped that the applicability and the reliability in computing the high-lift flows on unstructured mesh CFD is confirmed by improving the cost and accuracy.

The objectives of this study are to compare and assess structured and unstructured mesh CFD codes in simulating the flow around high-lift devices. Especially in three-dimensional computations, fewer comparisons between structured and unstructured mesh CFD were made because of complexity and high computational

Received 7 January 2005; presented as Paper 2005-1226 at the AIAA 43rd Aerospace Sciences Meeting and Exhibit, Reno, NV, 10–13 January 2005; revision received 29 March 2005; accepted for publication 29 March 2005.

*Researcher, Information Technology Center, Institute of Space Technology and Aeronautics, 7-44-1 Jindaiji-Higashi, Chofu. Member AIAA.
†Team Leader, Information Technology Center, Institute of Space Technology and Aeronautics, 7-44-1 Jindaiji-Higashi. Member AIAA.
‡Engineer, Engineering Solution Division, 2-19-13, Takanawa, Minato-ku.

costs. In this paper, computations of two-dimensional and three-dimensional high-lift configurations are performed, and the reliability is clarified. The following four computations are performed both on structured mesh and unstructured mesh, and the computational results are validated: 1) two-element (main and flap) airfoil, 2) three-element (slat, main, and flap) airfoil, 3) three-element (full-span slat, main, and full-span flap) wing with fuselage, and 4) three-element (full-span slat, main, and part-span flap) wing with fuselage. In the two-dimensional problems 1 and 2, detailed grid studies with mesh adaptation on unstructured mesh are performed. In the three-dimensional problems 3 and 4, some modest grid studies are performed with structured meshes caused by the high computational costs. By comparison with the results, ways to improve the reliability on structured and unstructured meshes are discussed.

II. Flow Solvers

As the flow solver on multiblock structured meshes, an in-house code, UPACS (Unified Platform for Aerospace Computational Simulation), is used. It is a standard CFD code in the Institute of Space Technology and Aeronautics of Japan Aerospace Exploration Agency.[11,12] In this study, full Navier–Stokes equations are solved on the multiblock structured meshes by a cell-centered finite volume method. The third-order scheme of Roe's flux difference splitting for convection terms is used. Time integration is carried out using the matrix-free Gauss–Seidel implicit method, in which further simplifications are introduced to a lower/upper symmetric Gauss–Seidel (LU-SGS) implicit method.[13] The multiblock structured mesh is generated with commercial software, Gridgen.

As the unstructured mesh generator and flow solver, TAS (Tohoku University Aerodynamic Simulation) codes[14] are used in this study. TAS_Mesh is a mesh generator with graphical-user-interface tools.[15,16] It can generate a triangular surface mesh with the advancing front method and tetrahedral volume mesh using Delaunay tetrahedral meshing,[17] as well as hybrid volume mesh composed of tetrahedrons, prisms, and pyramids for viscous flows with high Reynolds number.[18] The unstructured surface meshing using isotropic triangles is semi-automatic, and the volume mesh generation is fully automated. In TAS_Flow, Navier–Stokes equations are solved on the unstructured mesh by a cell-vertex finite volume method. The Harten-Lax-van Leer-Einfeldt-Wada (HLLEW) method[19] is used for the numerical flux computations. Second-order spatial accuracy is realized by a linear reconstruction of the primitive variables. The LU-SGS implicit method[20] is used for time integration.

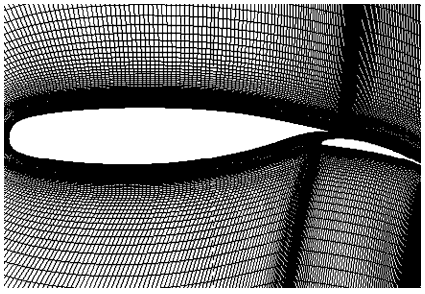

Fig. 1 Finest structured mesh for two-element NLR-7301 airfoil, *SG*-Fine.

In both codes, the Spalart–Allmaras (SA) turbulence model[21] is used in the present computations to simulate turbulent flows.

Computations are carried out on Fujitsu PRIMEPOWER HPC2500 multiprocessor, which is the main machine of Numerical Simulator III system in Institute of Space Technology and Aeronautics of Japan Aerospace Exploration Agency.[22]

III. Results

A. Two-Element (Main-Flap) Airfoil

1. *Model Geometry and Computational Conditions*

First, computations of a two-dimensional two-element airfoil are performed. The geometry used in this study is NLR-7301 airfoil[23] shown in Fig. 1. The model was tested in the NLR 3 m × 2 m low-speed wind tunnel in the 1970s, and the data can be obtained for validation of CFD in Ref. 23. The flap angle δF is set to a moderate value of 20 deg, and the gap width between main section and flap is 1.3% of c, where c is the chord of the basic NLR-7301 airfoil. The overlap of the main wing section and the flap O/L is 5.3% of c. The freestream Mach number is 0.185, and the Reynolds number is 2.51×10^6. The flow is assumed to be completely turbulent.

2. *Computational Results*

To examine the mesh dependency on structured meshes, three multiblock structured meshes, *SG*-fine, *SG*-Medium, and *SG*-Coarse, are generated. *SG*-Fine shown in Fig. 1 is a mesh whose outer boundaries are located 100 chord lengths away from the body surface. Flows around high-lift devices have large circulation and wake, so that the location of the outer boundary has a large influence, especially concerning drag prediction, as discussed in Ref. 24. Such computations require either a correction of the outer boundary conditions or a large computational domain. The minimum spacing in normal direction to the wing surface is 1×10^{-5}. The mesh has about 0.42 million mesh points. *SG*-Medium and *SG*-Coarse have $\frac{1}{4}$ and $\frac{1}{16}$ mesh points of *SG*-Fine, respectively, which are generated by removing mesh points from *SG*-Fine in both i and j direction, uniformly. Figure 2 shows the meshes near the leading edge of the main wing.

Figure 3 shows variations of lift coefficients C_l vs angle of attack α and C_l vs drag coefficients C_d as functions of mesh density. In the results on *SG*-Coarse, discrepancy in C_l appears near stall. C_d is also overpredicted. Discrepancy between *SG*-Fine and *SG*-Medium is little. At moderate angle of attack, C_l is not sensitive to mesh density. In Fig. 3b, the differences in C_d between *SG*-Fine and *SG*-Medium are only 3–10 drag counts (1 drag count $= 1 \times 10^{-4}$), and the mesh convergence for C_d can be seen. To validate the mesh convergence for C_d, the Richardson extrapolation[25] is used,

$$f[\text{exact}] \doteqdot 4/3 f_l - 1/3 f_2 \tag{1}$$

where f_1 and f_2 are solutions of fine mesh h_1 and coarse mesh h_2. The value is also shown in Fig. 4. It can be seen that the extrapolation predicts C_d convergence. The results on *SG*-Fine are very close to the converged results. Therefore, the results on *SG*-Fine are used in comparison with the results on unstructured meshes.

C_l-α and C_l-C_d computed by the baseline unstructured mesh *UG* are shown in Fig. 5. The baseline mesh shown in Fig. 6 has 1074 mesh points on the main element and 1476 points on the flap element.

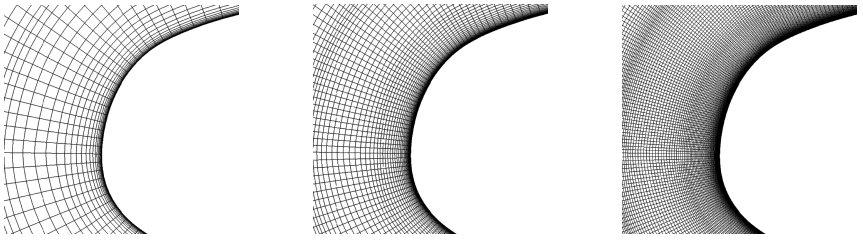

a) *SG*-Coarse **b) *SG*-Medium** **c) *SG*-Fine**

Fig. 2 Close-up view of structured meshes near the leading edge of the main wing.

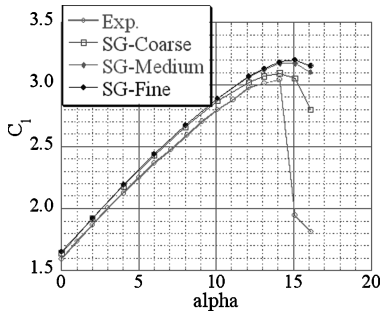

a) C_l-α

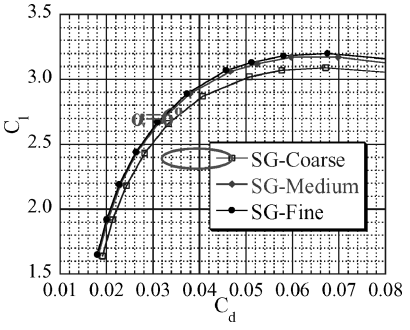

b) C_l-C_d

Fig. 3 Effect of mesh density on C_l-α and C_l-C_d for structured mesh (α, angle of attack; C_l, lift coefficient; C_d, drag coefficient).

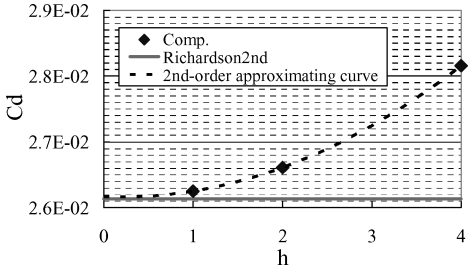

Fig. 4 Mesh convergence of C_d for structured meshes at $\alpha = 6$ deg.

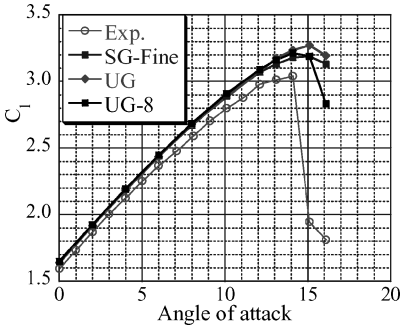

a) C_l-α

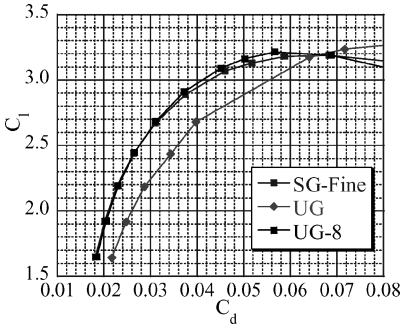

b) C_l-C_d

Fig. 5 Effect of mesh density on C_l-α and C_l-C_d for unstructured mesh.

On the blunt trailing edge there are about 25 mesh points. The minimum spacing in the normal direction to the wing surface is 1×10^{-5}. The mesh has about 0.08 million mesh points. Unstructured mesh is relatively easy to use local mesh refinement. Therefore, we start from coarser mesh points. In Fig. 5, C_l on *SG*-Fine and *UG* show almost the same behavior except near stall angle, whereas C_d for unstructured mesh is much larger compared to the computational results on *SG*-Fine. The difference at $\alpha = 6.0$ deg is about 80 drag counts, or more than 20%.

To examine the mesh dependency of C_d for unstructured meshes, a mesh-refinement method based on a bisection algorithm[26] is used. Selected mesh elements for mesh refinement are bisected, and mesh points are increased in the chosen regions. Regions that require more mesh points are investigated by changing regions for mesh refinement. The information of refined meshes is summarized in Table 1. Figure 7 shows the meshes.

Total, pressure, and friction drag coefficients (C_d, C_{dp}, and C_{df}) at $\alpha = 6.0$ deg obtained for each mesh are shown in Fig. 8. At all computations, the change of C_{df} is little. In *UG*-2, mesh points are increased in the regions near the flap wing, whereas in *UG*-3, the mesh points are increased in all regions two chord lengths away from the wing. The comparison of C_d between *UG*-2 and *UG*-3 shows that the result of *UG*-3 is significantly improved in drag prediction. C_d of *UG* is larger than that of *SG*-Fine by about 80 drag counts, whereas about 60 drag counts reduction of pressure drag can be seen in *UG*-3.

Next, to examine the effect of mesh density within two chord lengths, the following two meshes are used. *UG*-4 is obtained from *UG*-3 by increasing the mesh points in the region around the half of the main wing. *UG*-5 is obtained by further refinement in the same region as in *UG*-3. The difference in C_d between the results of *UG*-3, *UG*-4, and *UG*-5 is only a few drag counts, as shown in Fig. 8. Thus, we conclude that the mesh density of *UG*-3 within two chord lengths away from the wing is sufficient.

UG-3, *UG*-6, *UG*-7, and *UG*-8 are computational meshes, where the refined regions are extended to 2, 4, 20, and 50 chord lengths away from the wing. Compared to the result on *UG*, pressure drag is reduced by about 60, 70, and 80 drag counts, respectively. Difference in C_d between *UG*-7 and *UG*-8 is within one drag count.

Table 1 Refined regions of unstructured mesh

Mesh	Mesh points ($\times 10^6$)	Refined regions
UG	0.08	Baseline mesh for mesh refinement
UG-2	0.13	Near flap
UG-3	0.20	Two-chord lengths away from main airfoil
UG-4	0.35	Around the half of main airfoil in UG-3
UG-5	0.50	Two-chord lengths away from main airfoil in UG-3
UG-6	0.23	Four-chord lengths away from main airfoil
UG-7	0.25	20 chord lengths away from main airfoil
UG-8	0.25	50 chord lengths away from main airfoil
UG-9	0.14	Mesh points on airfoil are double as many as UG
UG-10	0.33	50 chord lengths away from main airfoil in UG-9

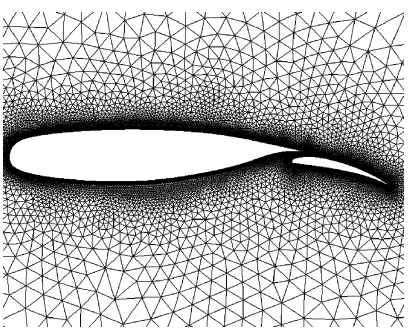

Fig. 6 Baseline unstructured mesh for two-element NLR-7301 airfoil, *UG*.

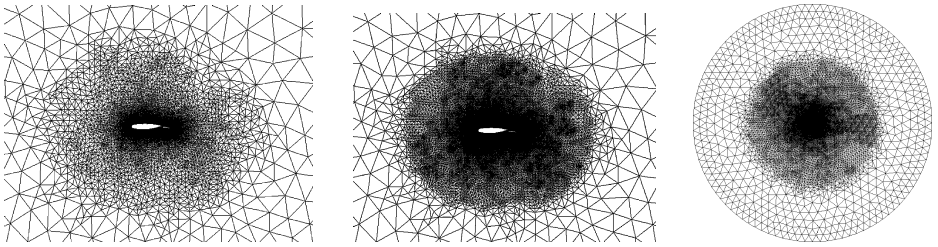

a) *UG*-3 b) *UG*-5 c) *UG*-8

Fig. 7 Refined unstructured meshes.

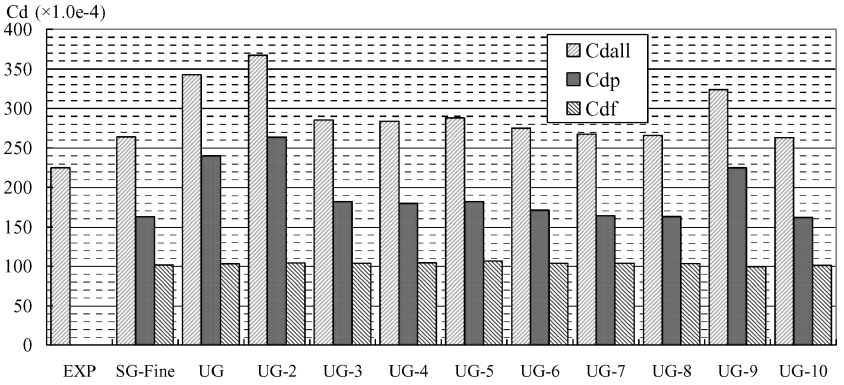

Fig. 8 Comparison of drag components at $\alpha = 6$ deg (Cdall, total drag; Cdp, pressure drag; Cdf, friction drag).

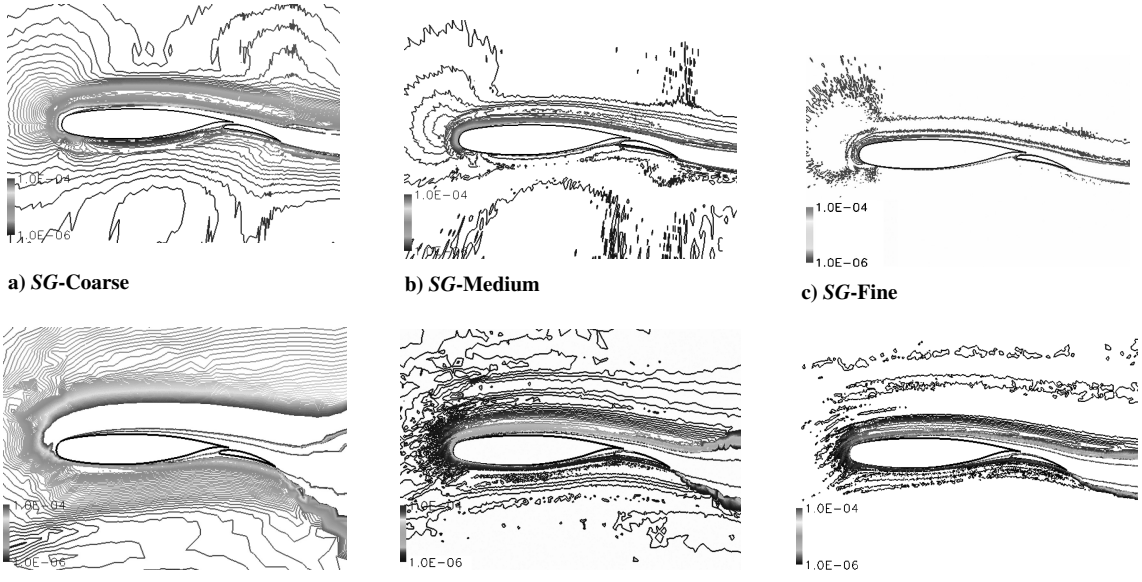

a) *SG*-Coarse b) *SG*-Medium c) *SG*-Fine

d) *UG* e) *UG*-3 f) *UG*-8

Fig. 9 Contours of entropy variation change. (The range of contours is from 10^{-6} to 10^{-4}.)

These results show the importance of the mesh density away from the wing.

On *UG*-9 and *UG*-10, the number of the mesh points on the main element and flap element of *UG* is doubled. As shown in Fig. 8, however, the differences of C_D between *UG* and *UG*-9 are not so large, and results on *UG*-8 and *UG*-10 are almost same. Again, it shows the importance of the mesh density away from the wing surface.

Figure 9 shows the contours of entropy change, which is defined as follows:

$$\Delta s/R = [1/(\gamma - 1)]\, \ell_n \left[(p/p_\infty)(\rho_\infty/\rho)^\gamma \right] \qquad (2)$$

where p, ρ, and γ are pressure, density, and specific heat ratio, respectively. The subscript ∞ represents the value of the physical variables in freestream. In general, entropy increment can be seen in the boundary layers and after the generation of shock waves. In Figs. 9a and 9d, it can be seen that numerical error results in nonphysical increase in entropy in the regions far away from the wing surface. On *SG*-Coarse mesh, entropy increment appears nonphysically and the value is decreased at finer meshes. On *UG* mesh, nonphysical increment of entropy is especially large, a clear evident of lack of mesh resolution. By extending the refinement region, the entropy increment becomes smaller, as shown in Figs. 9e and 9f.

On unstructured meshes, the mesh tends to become coarser rapidly in the regions away from the wing surface. Because flows around high-lift devices have large circulation and wake, they still

change in the regions away from the wing surface. If the mesh size in the region is too large, the flow changes cannot be captured, and loss of total pressure and nonphysical production of entropy will occur. In comparison, structured meshes have higher density away from the wing surface because of its topology, which helps to capture the flow variation.

Figure 5 shows the comparison of C_l-α and C_l-C_d for *SG*-Fine, *UG*, and *UG*-8. By proper distributions of mesh points, the results of unstructured meshes are comparable to those of fine structured mesh. In this study, wide refinement regions are selected to investigate the mesh dependency. Observing the decrease in entropy increment suggests that it can be used as mesh-refinement indicator.

B. Three-Element (Slat-Main-Flap) Airfoil

1. *Model Geometry and Computational Conditions*

In this section, more complicated flows with the slat are computed. The configuration used in this study is composed of a slat, main airfoil, and single-slotted flap, as in Ref. 27. The slat and flap angle are set to 25 and 20 deg, respectively. This configuration was used as a code validation challenge by the CFD Society of Canada[28] in 1996. The freestream Mach number is 0.197, and the Reynolds number is 3.52×10^6. In the experiments, transition from laminar to turbulent on the main element is forced at $x/c = 0.125$ on both the upper and lower surface. On the slat and flap, transition is free. In the computations, transition is fixed on the main wing as specified in the experiment. On the slat and flap, fully turbulent flow is assumed.

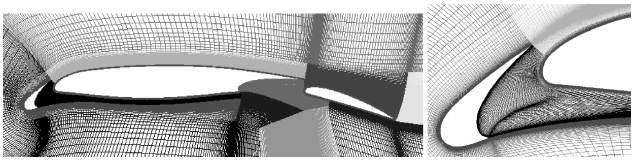

Fig. 10 Multiblock structured mesh of three-element airfoil.

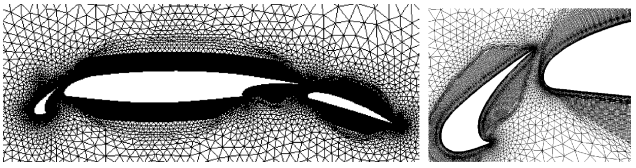

Fig. 11 Baseline unstructured mesh of three-element airfoil, Mesh 1.

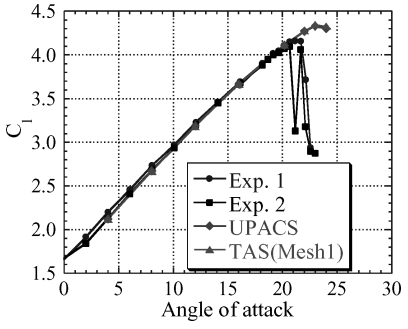

a) C_l-α

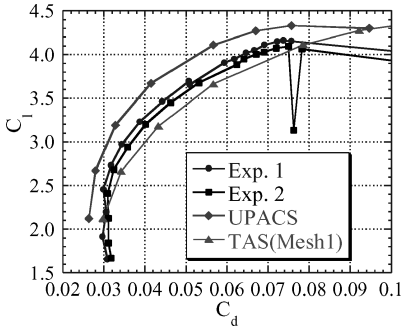

b) C_l-C_d

Fig. 12 Comparison of C_l-α and C_l-C_d between wind-tunnel results and computational results.

The computational meshes used in this study are shown in Figs. 10 and 11. The minimum spacing in the normal direction to the wing surface is 5×10^{-6} on both structured and unstructured meshes. The multiblock structured mesh has 26 blocks and 143,032 mesh points. The outer boundary is located 100 chord lengths away from the body surface. The unstructured mesh is a baseline mesh that is not adapted to the wake and has 45,997 mesh points. The outer boundary is located 100 chord lengths away from the body surface. For both structured and unstructured meshes, the surface mesh points and distributions on wing are almost the same, except near the trailing edges, where there are more mesh points in the unstructured mesh.

Regarding unstructured mesh, the baseline mesh and three refined meshes are used to examine the effect of mesh dependency, as summarized in Table 2. The details are described in the following section.

2. *Computational Results*

Figures 12a and 12b show variations of lift coefficients C_l vs angle of attack α and C_l vs drag coefficients C_d. Figures 13 and 14 show computed Mach contours at $\alpha = 4.01$ deg.

Regarding C_l-α, both computational results show almost the same behavior even near stall angle. The difference in C_l does not exceed 1.0%, and the average is about 0.5%, which is considered reasonable. Compared with experimental results,[27] computational results show excellent agreement everywhere, except for stall, where a delay of 2–3 deg is observed. The delay is perhaps caused by the relatively larger eddy viscosity in flow separation produced by the SA turbulence model.

Table 2 Unstructured mesh refinement for the case of three-element airfoil

Mesh	Mesh points	Refined regions
Mesh 1	45,997	Baseline mesh for mesh refinement
Mesh 2	75,083	50 chord lengths away from main airfoil in Mesh 1
Mesh 3	117,621	Mesh adapted to the result at $\alpha = 4.01$ deg ($\approx$Mesh 2 + Wake)
Mesh 4	170,751	Mesh adapted to the result at $\alpha = 20.18$ deg

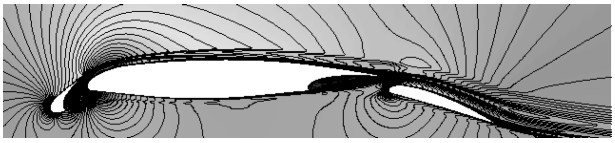

a) Structured mesh

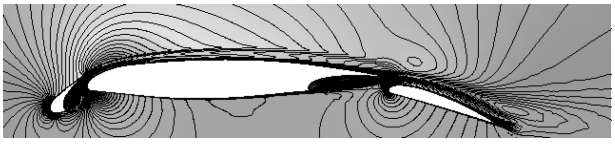

b) Baseline unstructured mesh, Mesh 1

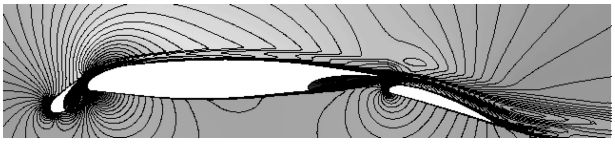

c) Refined unstructured mesh, Mesh 3

Fig. 13 Mach contour at $\alpha = 4.01$ deg.

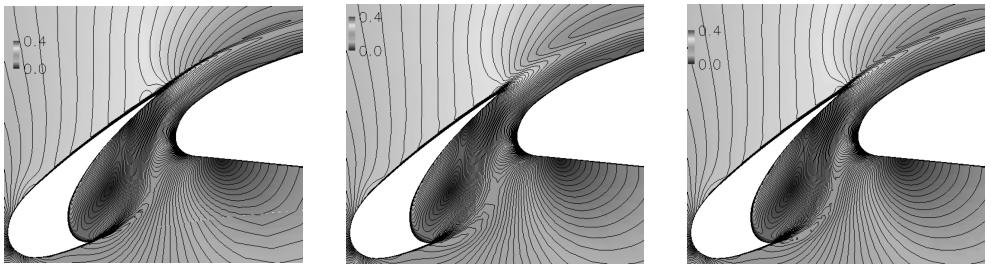

a) Structured mesh **b) Baseline unstructured mesh, Mesh 1** **c) Refined unstructured mesh, Mesh 3**

Fig. 14 Mach contour around slat at $\alpha = 4.01$ deg.

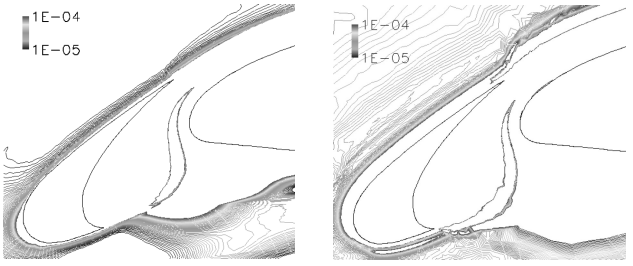

a) Structured mesh **b) Baseline unstructured mesh, Mesh 1**

Fig. 15 Contours of entropy change near the slat at $\alpha = 4.01$ deg.

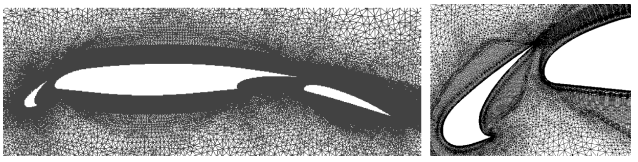

Fig. 16 Refined unstructured mesh, Mesh 3.

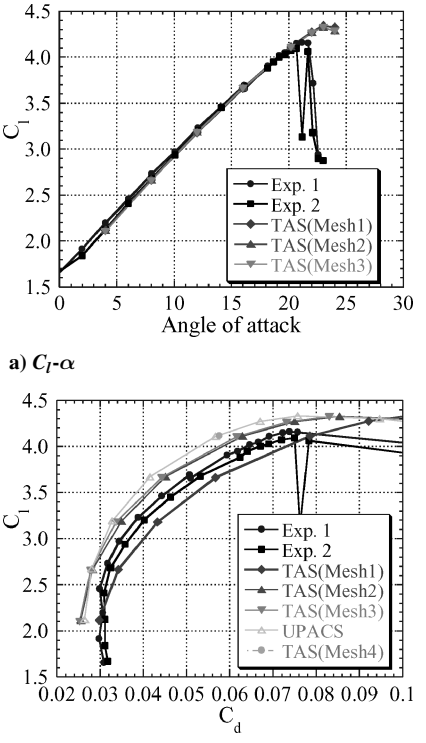

a) C_l-α

b) C_l-C_d

Fig. 17 Effect of mesh density on aerodynamic forces for unstructured mesh.

Regarding C_l-C_d, C_d for unstructured mesh is much larger compared to the computational results on the structured mesh, although it shows better agreement with experimental data. Figure 15 shows the entropy contour near the slat. In Fig. 15b, the entropy is nonphysically increased in the regions away from the wing surface because of the numerical error in unstructured mesh, which indicates insufficient mesh resolution. Again, a mesh-refinement method is utilized to examine mesh dependency. The original unstructured mesh, Mesh 1, is used as the baseline mesh.

The mesh refinement is summarized in Table 2. The results in the preceding section showed that sufficient mesh density away from the wing surface is required for accurate drag prediction to handle large circulation in the flow around a high-lift device. In Mesh 2, mesh points are increased within 50 chord lengths away from the wing. In Mesh 3, mesh resolution in wake regions at $\alpha = 4.0$ deg is also improved using entropy increment as the mesh-refinement indicator. Figure 16 shows Mesh 3. Using this approach, we can identify the regions of physical importance as well as those where numerical error should be decreased.

Figures 17a and 17b show C_l-α and C_l-C_d as functions of unstructured mesh density. The difference in C_l-α is very small except for $C_{l\max}$, whereas in C_d a large improvement can be seen. Regarding C_l-C_d, the difference in C_d is still large at higher angle of attack. At this condition, the flow on the upper side of the slat is greatly accelerated. In fact, it can even exceed sonic speed. In addition, the wake of the slat shifts away from the wing surface and enters the region of insufficient mesh resolution. The mesh is then readapted to the wake at a higher angle of attack, and the mesh density near the slat is increased (Mesh 4) using entropy increment as the mesh-refinement indicator. As indicated by the result at $\alpha = 20.18$ deg, C_d is considerably reduced to almost the same value as that of the structured mesh. At higher angle of attack, more mesh points were required to capture the accelerated flow on the upper side of the slat and the distant wake. When the flow characteristics can be changed largely, the grid should be readapted.

Computed surface-pressure coefficients C_p are compared with experimental results at $\alpha = 4.01$ deg in Fig. 18. Both computational results show good agreement with experimental data on all airfoil elements.

Boundary layer and wake profiles of total pressure coefficient C_{p0} are compared in Figs. 19 and 20. The profiles are taken at a line normal to the upper surface at $x/c = 0.35$ on the main element and at $x/c = 1.214$ on the flap (trailing edge). The variable d is the normal distance from the airfoil surface. Figures 19a and 20a show the total pressure loss caused by the boundary layer on the main wing and the wake from the slat. In Figs. 19b and 20b, the merging of the wakes from the slat and main element can be seen.

On the original unstructured mesh, Mesh 1, the wake is highly diffused. Using the present mesh-refinement method, the diffusion is suppressed, and the profile is significantly improved. The computational results on the structured and refined unstructured meshes show the similarity with experimental results[27] and with each other. The detail in flow physics is well resolved on unstructured mesh because of proper distribution of mesh points in the regions of

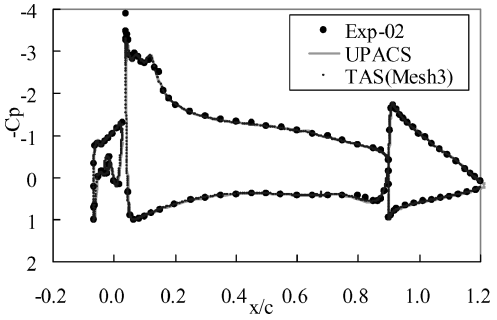

Fig. 18 Surface-pressure coefficients C_p at $\alpha = 4.01$ deg.

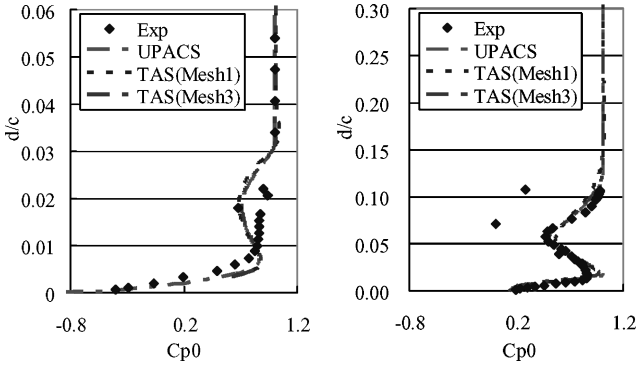

a) $x/c = 0.35$ **b) $x/c = 1.214$**

Fig. 19 Boundary layer and wake profiles of total pressure coefficient C_{p0} at $\alpha = 4.01$ deg (d, normal distance from the airfoil surface).

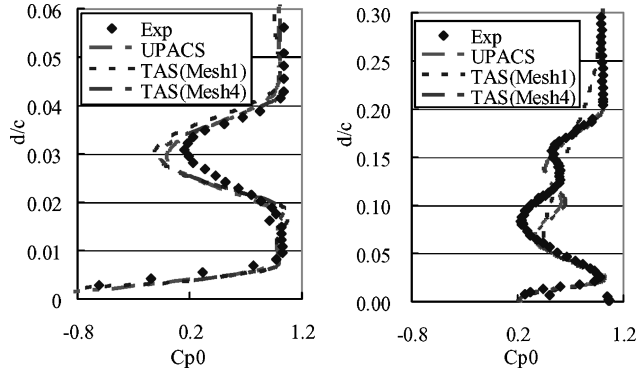

a) $x/c = 0.35$ **b) $x/c = 1.214$**

Fig. 20 Boundary layer and wake profiles of C_{p0} at $\alpha = 20.18$ deg.

physical importance, such as the wake and region where gradient of flow variables is large, as well as those where numerical errors should be decreased using entropy increment as the mesh-refinement indicator.

C. Three-Element (Slat-Main-Flap) Wing and a Fuselage

1. Model Geometry and Computational Conditions

In this section, two kinds of trapezoidal high-lift wing models[29,§] are computed both on multiblock structured and unstructured meshes, as shown in Figs. 21 and 22. One is a full-span flap model that has a full-span slat and a full-span single-slotted flap that extend from wing root to wing tip. The other is a part-span flap model that has a full-span slat and a part-span flap that has a span equal

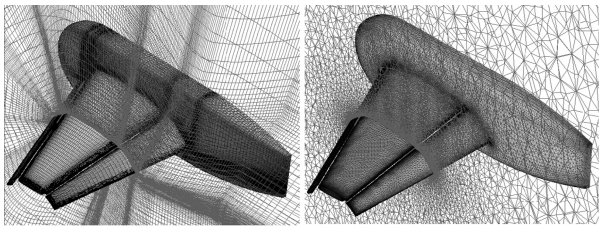

a) Distant view

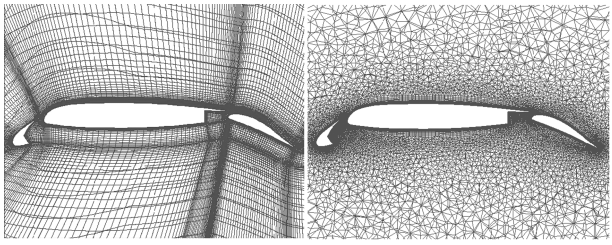

b) Cross-sectional view at 50% span

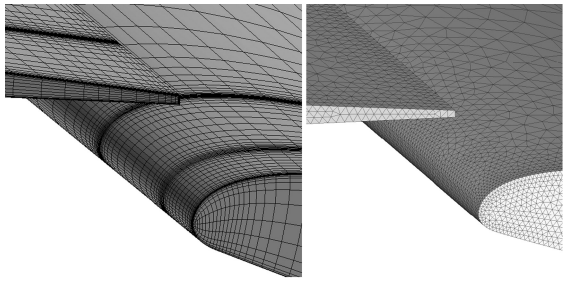

c) Close-up view near leading edge of flap

Fig. 21 Computational mesh of three-element trapezoidal wing with a full-span flap: left, structured mesh and right, unstructured mesh.

to roughly half of the span length of the model. The models were tested at NASA Langley in 1998 and NASA Ames in 1999. The experiments using the models were performed to produce experimental data for validation and development of CFD methods for three-dimensional high-lift flows.[29,§] In the wind-tunnel tests, the models have a variety of slat and flap settings. In this study, a setting for landing is used for both configurations. The slat and flap deflections are 30 and 25 deg, respectively. The mean aerodynamic chord of the model c is 39.6 in. (1 m), and the model semispan is 85.1 in. (2.16 m). The slat gap and slat height are $0.015c$. The flap gap and flap overlap are $0.015c$ and $0.005c$, respectively.

For each configuration, a structured mesh and an unstructured mesh are generated, as shown in Figs. 21 and 22. The minimum spacing in the normal direction to the wing surface is $0.01/\sqrt{Re}$ on unstructured meshes and $0.02/\sqrt{Re}$ on structured meshes. The outer boundary is a semisphere, whose radius is about $60c$. The multiblock structured meshes were generated with the commercial software, Gridgen. The total number of mesh points is about 7.5 million for the full-span model and 9.8 million for the part-span model. The number of blocks is 586 blocks for the full-span model and 848 blocks for the part-span model. More than one month is required to generate the mesh by an expert for each configuration. To study mesh dependency, a fine mesh for the full-span configuration, which has about eight times mesh points of the baseline mesh, is also generated by adding mesh points in the i, j, and k direction, uniformly. The unstructured meshes were generated with TAS-Mesh. The meshes have about 13 million mesh points in volume mesh at both configurations. To generate the unstructured meshes from CAD data, only a few days are required. The unstructured surface meshing using isotropic triangles is semi-automatic, and it took only a few hours. However, it requires a large number of mesh points at leading-edge and trailing-edge sections. The trailing edges of this model are blunt and very thin. To insert sufficient number of mesh points using isotropic triangles, a huge number of mesh points is required. Therefore, the trailing edges have

§Data available online at http://db-www.larc.nasa.gov/trapwing/archive/register [cited 5 Jan. 2005].

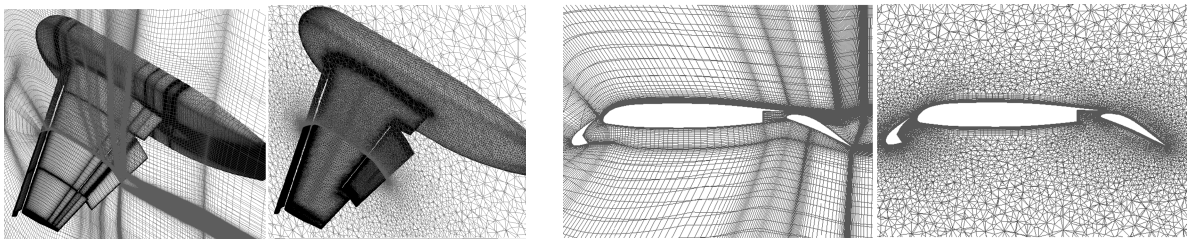

a) Distant view

b) Cross-sectional view at 50% span

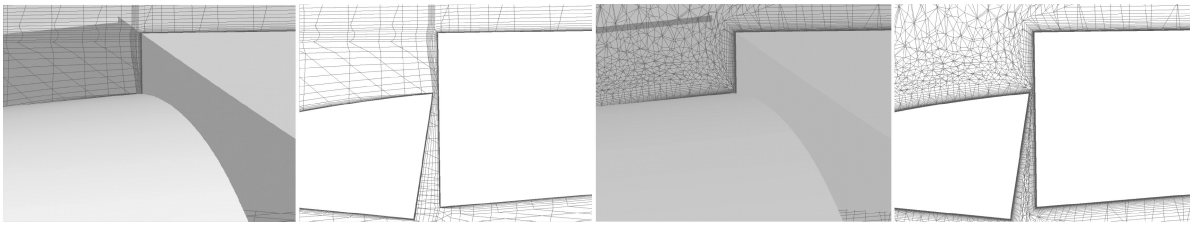

c) Cross-sectional view near a gap between the main and flap wing

Fig. 22 Computational mesh of three-element trapezoidal wing with a part-span flap (left, structured mesh; right, unstructured mesh).

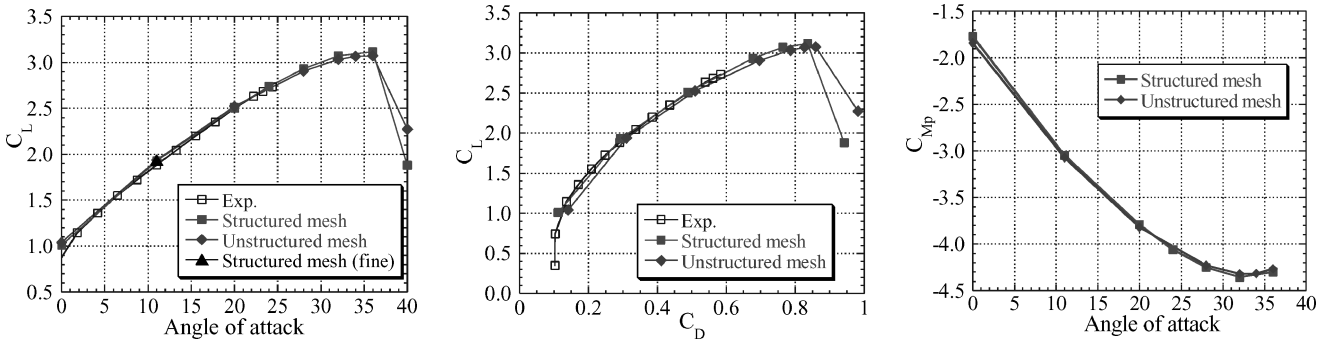

a) C_L-α b) C_L-C_D c) C_{Mp}-α

Fig. 23 Comparison of C_L-α, C_L-C_D, and C_{Mp}-α between wind-tunnel results and computational results. (C_{Mp}-α does not include the experimental results.)

only one or two elements for the unstructured meshes as shown in Fig. 21c, compared to about six elements for the structured meshes.

In the current computations, the freestream Mach number is 0.15, and the Reynolds number is 15×10^6. Fully turbulent flows are assumed in the computations.

2. *Computational Results of Full-Span Flap Configuration*

Figures 23a and 23b show C_L-α and C_L-C_D for computed results and experimental data.[§] Figure 23c shows C_{Mp} (pitching-moment coefficient)-α for computed results. As for C_L-α, although both computational results predict slightly higher C_L (about 1%), the results show good agreement with the experimental data at the moderate angles of attack. The difference between computations in C_L at the moderate angle of attack is 1.0%, and the difference in $C_{L\max}$ is 1.4%, which is considered reasonable. In the published date at the website,[§] the experimental data near the stall angle of attack are not available. Therefore, compared with the experimental and computational results in Ref. 8, a stall delay of 2–3 deg is observed in our computations. As for C_M-α, the difference between computational results does not exceed 1% at almost all angles of attack. As for C_L-C_D, the overall level and the tendency of both computational results agree well with the wind-tunnel results. However, differences between computations in C_D are relatively larger. The differences are about 200–300 drag counts, which is about 3–6%.

[§]Data available online at http://db-www.larc.nasa.gov/trapwing/archive/register [cited 5 Jan. 2005].

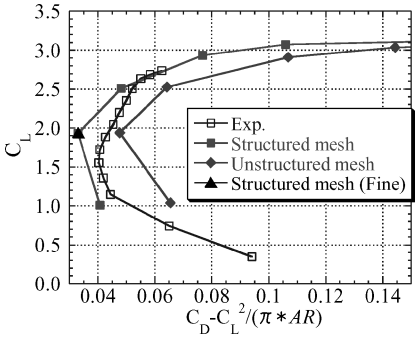

Fig. 24 Comparison of C_L-$C_{D\text{profile\_ideal}}$ between wind-tunnel results and computational results.

In Fig. 24, the estimated profile drag coefficients $C_{D\text{profile\_ideal}}$ are compared. The value is obtained by subtracting the ideal induced drag $C_L^2/\pi/AR$, from C_D, where AR is the aspect ratio of the wing. The ideal induced drag can be more than 85% of the total drag. In the three-dimensional case, the induced drag is so large that the difference in C_D between structured and unstructured meshes seems less than that in the preceding two-dimensional cases. Comparing the computational results in Fig. 24, however, the estimated $C_{D\text{profile\_ideal}}$ for unstructured mesh is much higher.

In Fig. 25, C_D at angle of attack of 11.02 deg is broken down into some components, such as C_{Dp} and C_{Df} to investigate the differences. The results for fine structured mesh are also shown here. The

percentage of pressure drag is more than 95% in the total drag. The difference between the original and fine structured meshes in C_{Dp} and C_{Df} is only 20 drag counts and two drag counts, respectively. The differences between unstructured mesh and fine structured mesh in C_{Dp} and C_{Df} is about 150 drag counts (≈4%) and five drag counts (≈5%), respectively.

Figures 26 show a comparison of C_P at $\alpha = 11.02$ deg. Both computational results are in good agreement with wind-tunnel results except for slat components, especially near its leading edge, whereas the computational results agree with each other. One possible cause is the difference in the stagnation-point location on the slat because the flow in the experiment is inclined as a result of the wind-tunnel wall interferences. In Fig. 26, differences of C_P distribution between computational results can also be seen near the trailing edge and the wing tip. C_P on unstructured mesh has a large jump at all trailing edge. It is conceivable that the jump is caused by the lack of mesh points near the blunt trailing edge, which affects the circulation and aerodynamic forces. In addition, larger differences in C_p can be seen in all computations near the wing tip where large vortices are generated, as shown in Fig. 27. The strength of the wing-tip vortices is different in the computations. The difference is caused by mesh resolution, and it affects C_p near the wing tip.

Figures 28 shows the computed Mach contours at 50% span location. Overall flow structures are almost the same except for the wake regions. On the unstructured mesh, the wake on the flap is spread out. However, the computed aerodynamic forces show fair agreement with experimental results. At these moderate angles of attack and relatively moderate settings of slat and flap, the slat effects to aerodynamic forces are not very important. However, the lack of mesh resolution for the wakes can lead to inaccurate lift and stall prediction as the angle of attack and the deflection of the slat and flap are increased. In addition, the unresolved wakes result in higher drag. Mesh-refinement approaches that insert highly dense mesh in the slat wake and the use of adaptive mesh refinement must be required for more accurate prediction of the flow physics.

Figure 29 shows the surface-restricted streamlines at $\alpha =$ 20.18 deg. Compared with Figs. 29a and 29c, the overall flow pattern is similar, but a large difference can be seen in the corner flow near the junction of the wing and body. In this configuration, there is no fairing at the junction. Flow separation can be observed at this corner. It is very sensitive to mesh resolution and turbulence model, as discussed in Ref. 12. On structured mesh, stretched elements in the spanwise direction are generally used. Therefore, the mesh resolution becomes relatively coarser at the corner on the wing.

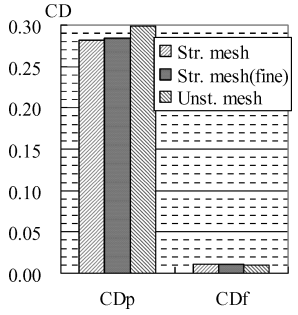

Fig. 25 Comparison of drag components between computational results on structured and unstructured mesh at $\alpha = 11.02$ deg (CDp, pressure; CDf, friction).

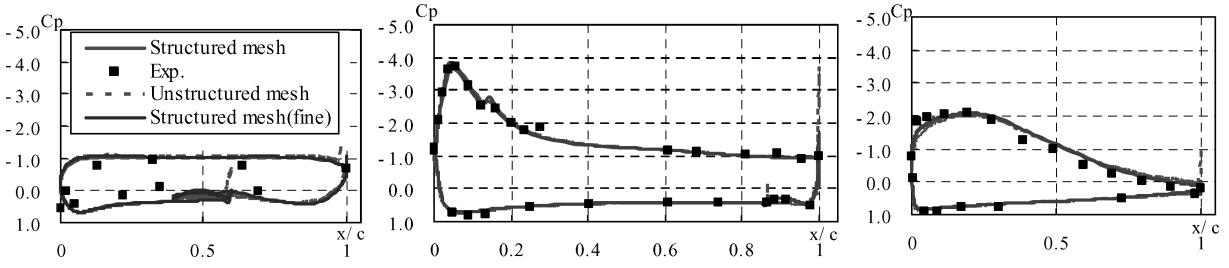

a) 50% span

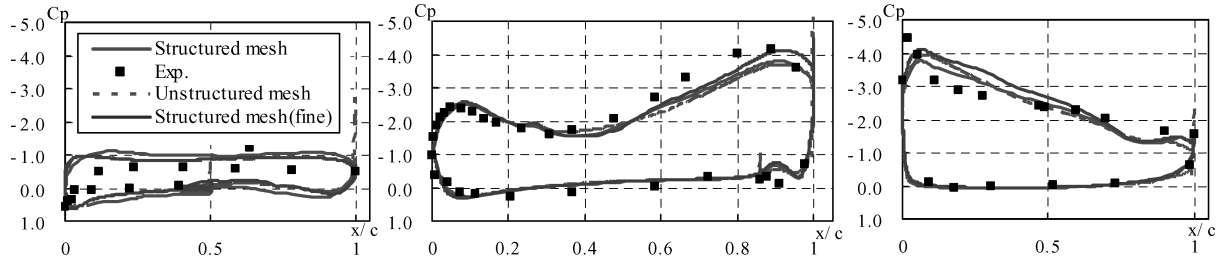

b) 98% span

Fig. 26 Comparison of C_P at $\alpha = 11.02$ deg at each span location (left, slat; center, main wing; right, flap).

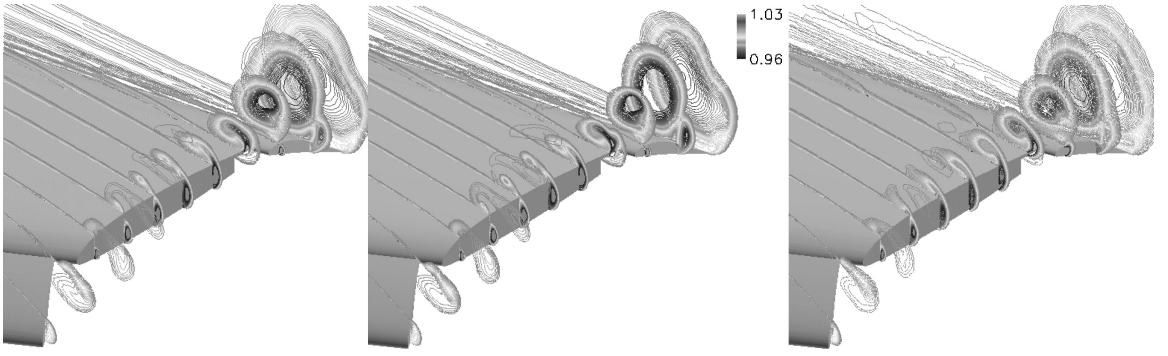

a) Structured mesh **b) Fine structured mesh** **c) Unstructured mesh**

Fig. 27 Total pressure contours near wing tip at $\alpha = 11.02$ deg.

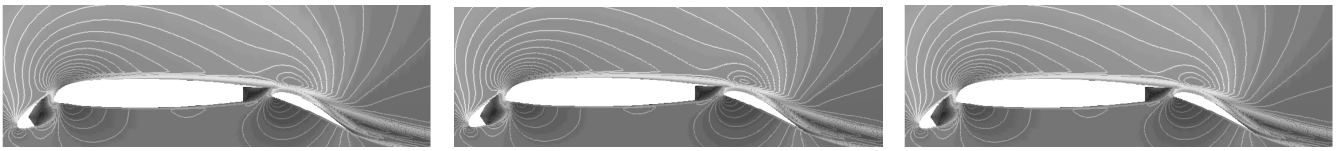

a) Structured mesh b) Fine structured mesh c) Unstructured mesh

Fig. 28 Mach contours at 50% span location ($\alpha = 11.02$ deg).

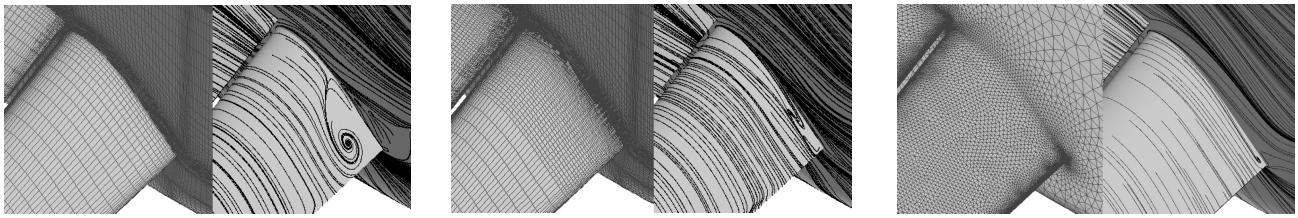

a) Baseline structured mesh b) Refined structured mesh near the junction c) Unstructured mesh

Fig. 29 Surface-restricted streamlines at $\alpha = 20.18$ deg.

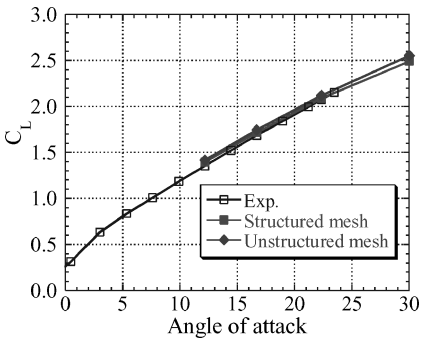

a) C_L-α

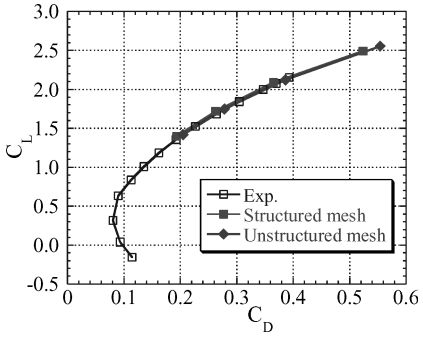

b) C_L-C_D

Fig. 30 Comparison of C_L-α and C_L-C_D between wind-tunnel results and computational results.

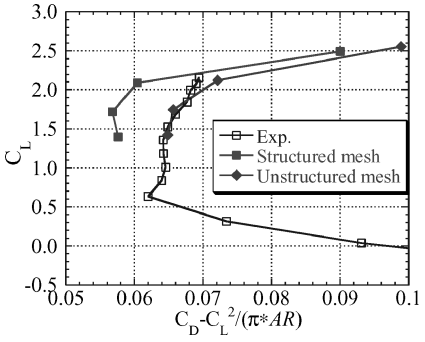

Fig. 31 Comparison of C_L-$C_{D\text{profile\_ideal}}$ between wind-tunnel results and computational results.

Figure 29b shows the results on a structured mesh where mesh resolution near the junction is significantly enhanced. As the result, the size of the flow separation becomes smaller, and the similarity with the results of unstructured mesh is improved. By refining the mesh, 1% changes in C_L and C_D are obtained. This emphasizes the importance in quantitative prediction of the flow separation at such corner.

3. Computational Results of Part-Span Flap Configuration

Figures 30a and 30b show C_L-α and C_L-C_D for computed results and experimental data. Figure 31 shows estimated $C_{D\text{profile\_ideal}}$. For this part-span flap configuration, as for C_L-α, the difference between the computational results and experimental results becomes slightly larger than that for the full-span flap configuration. The computational results on the structured mesh and unstructured mesh overestimate C_L by about 1.8 and 3.3%, respectively. The difference between the computational results is about 1.5%. As for C_L-C_D, the overall level and the tendency of both computational results agree well with experimental results. The differences are about 100–200 drag counts, which is about 5%. Comparing the computational results in Figs. 30b and 31, it is found that the results on the unstructured mesh show better agreement with experimental data. However, the estimated $C_{D\text{profile\_ideal}}$ by unstructured mesh is higher, and the results show the same tendency with the computations of full-span flap configuration.

Figure 32 shows a comparison of C_P distribution at $\alpha = 16.70$ deg. At midspan of the flap, computational results agree well with wind-tunnel results. The difference between computations is little, except for the trailing edge as discussed in the full-span flap case. On the other hand, near the tip of main wing and flap, the difference arises because of the tip vortices. Figure 33 shows the total pressure contours at $\alpha = 16.70$ deg. On the structured mesh, the wing-tip vortices are slightly diffused at the upper side of the main wing compared to that of the unstructured mesh, as shown in Fig. 33a. For the structured mesh, a large number of mesh points is required to generate a mesh in the region of the part-span flap. The mesh density becomes relatively coarser at the wing tip. Near the wing tip of the flap in Fig. 33b, slight discrepancies can be also seen where the flow physics becomes more complex as a result of the gap.

Fortunately, it is shown that reasonable values of aerodynamic forces can be predicted using the unstructured mesh at moderate settings of slat and flap, despite minor differences in local flow physics. At a larger deflection angle, however, the effect of local flow physics is expected to become larger, following the increase in aerodynamic load. Computations and further mesh-refinement study to resolve the tip vortices and wakes must be required to acquire better knowledge in such case.

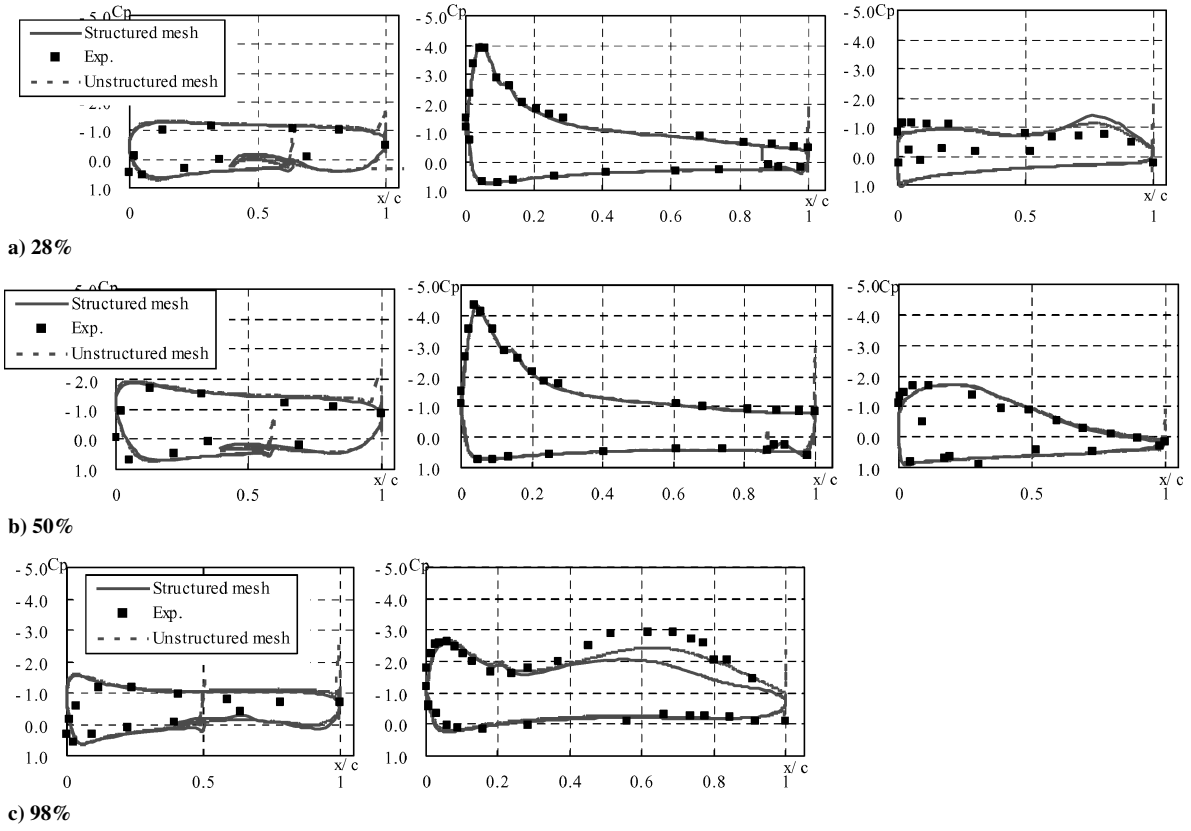

Fig. 32 Comparison of C_P at $\alpha = 16.70$ deg at each span location (left, slat; center, main wing; right, flap).

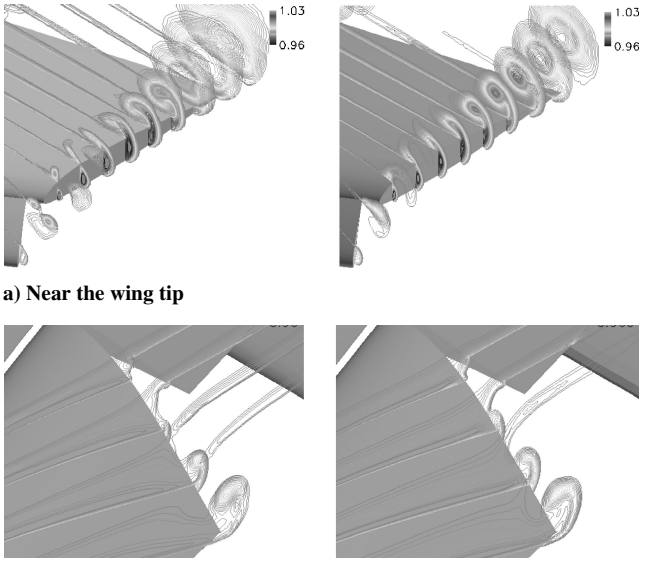

Fig. 33 Total pressure contours near wing tip at $\alpha = 16.70$ deg (left, structured mesh; right, unstructured mesh).

IV. Conclusions

To assess and improve the reliability of aerodynamic force prediction in the flow simulation around high-lift devices on multiblock structured and unstructured mesh, computations of two-dimensional and three-dimensional high-lift configurations have been performed. In the two-dimensional problems, detailed grid studies with mesh adaptation on unstructured mesh have been performed. In the three-dimensional problems, some modest grid studies have been performed with structured meshes because of the high computational costs.

First, computations for a two-element NLR-7301 airfoil were performed. C_l was less sensitive to mesh density, and the difference was little on structured and unstructured meshes, whereas the difference in C_d was very large. Mesh dependency with respect to C_d for unstructured meshes was examined using a mesh-refinement approach. Various refinement regions were used to investigate the difference in computed drag coefficients on a structured and an unstructured mesh. It was shown that the mesh density away from the wing surface was required for drag prediction because the flows around high-lift devices had large circulation and wake. Nonphysical entropy was produced in the regions away from the wing surface, where the mesh size was too large to capture the changes in flow properties.

Next, more complicated two-dimensional flows with slat were computed. A mesh-refinement approach using entropy increment as the refinement indicator was applied. The method was effective in increasing mesh points in the regions of physical importance, such as wake and the region where numerical error should be decreased. Again, C_l was less sensitive to mesh density. C_d was overestimated, and wake diffusion on the unstructured mesh was siginificantly improved. The results on the unstructured mesh became comparable with those of the multiblock structured mesh. By proper distribution of mesh points on unstructured mesh, the detail in flow physics was well resolved.

Computations of three-dimensional three-element trapezoidal wings with fuselage were also performed. Two configurations with full-span flap and part-span flap were used. Some minor differences of local flow physics, such as the resolution of the wake and wing-tip vortices were seen. However, reasonable prediction of aerodynamic forces was obtained even on the unstructured mesh, when the moderate settings of slat and flap were used. In both configurations, C_L was predicted well both on structured and unstructured mesh. The difference between computations was 1.5% at most. Surface-pressure distributions were also predicted well except near the wing and flap tip. The overall level and tendency of C_D also agreed well with wind tunnel and with each other. The difference between computations in C_D was relatively larger, which was an average of 5%. Because these configurations produced high lift, the total drag might comprise ideal

induced drag of more than 85%. In the three-dimensional case, the induced drag was so large that the difference in C_D between structured and unstructured meshes seemed less than in the preceding two-dimensional cases. However, the estimated $C_{D\text{profile\_ideal}}$ for unstructured mesh was much higher. Further mesh-refinement study needs to be conducted in the same manner as in the two-dimensional cases, especially for precise drag prediction.

In this study, local flow physics does not seem to affect the aerodynamic forces significantly. However, as the deflection angle of the slat and flap becomes larger and the flap produces much larger load, the effect is expected to increase. To improve the results, issues such as turbulence and transition modeling need to be addressed. However, at the same time we need to consider the effect of mesh quality. Computations and further mesh refinement to resolve the regions containing wake, wing-tip vortices, trailing edge, and the flow separation at the wing-body juncture must be required to acquire better knowledge in high-lift devices.

References

[1]Meredith, P. T., "Viscous Phenomena Affecting High-Lift Systems and Suggestions for Future CFD Development," *High-Lift Systems Aerodynamics*, AGARD CP-515, Sept. 1993, pp. 19-1–19-8.

[2]Kim, S., Alonso, J., and Jameson, A., "Multi-Element High-Lift Configuration Design Optimization Using Viscous Continuous Adjoint Method," *Journal of Aircraft*, Vol. 41, No. 5, 2004, pp. 1082–1097.

[3]Kim, H.-J., Obayashi, S., and Nakahashi, K., "Flap-Deflection Optimization for Transonic Cruise Performance Improvement of Supersonic Transport Wing," *Journal of Aircraft*, Vol. 38, No. 4, 2001, pp. 709–717.

[4]Jeong, S., Murayama, M., and Yamamoto, K., "Efficient Optimization Design Method Using Kriging Model," *Journal of Aircraft*, Vol. 42, No. 2, 2005, pp. 413–420.

[5]Rumsey, C. L., and Ying, S. X., "Prediction of High Lift: Review of Present CFD Capability," *Progress in Aerospace Science*, Vol. 38, No. 2, 2002, pp. 145–180.

[6]Hansen, H., et al., "Overview About the European High Lift Research Programme EUROLIFT," AIAA Paper 2004-0767, Jan. 2004.

[7]Nash, S. M., and Rogers, S. E., "Numerical Study of a Trapezoidal Wing High-Lift Configuration," Society of Automotive Engineers, Paper 1999-01-5559, Oct. 1999.

[8]Rogers, S. E., Roth, K., and Nash, S. M., "Validation of Computed High-Lift Flows with Significant Wind-Tunnel Effects," *AIAA Journal*, Vol. 39, No. 10, 2001, pp. 1884–1892.

[9]Murayama, M., Nakahashi, K., and Matsushima, K., "A Robust Method for Unstructured Volume/Surface Mesh Movement," *Transactions of the Japan Society for Aeronautical and Space Sciences*, Vol. 46, No. 152, Aug. 2003, pp. 104–112.

[10]Murayama, M., Nakahashi, K., and Sawada, K., "Simulation of Vortex Breakdown Using Adaptive Grid Refinement with Vortex-Center Identification," *AIAA Journal*, Vol. 39, No. 7, 2001, pp. 1305–1312.

[11]Takaki, R., Yamamoto, K., Yamane, T., Enomoto, S., and Mukai, J., "The Development of the UPACS CFD Environment," *High Performance Computing, Proceedings of the 5th International Symposium of ISHPC 2003*, edited by Vie-denbaum et al., Springer-Verlag, 2003, pp. 307–319.

[12]Yamamoto, K., Ochi, A., Shima, E., and Takaki, R., "CFD Sensitivity of Drag Prediction on DLR-F6 Configuration by Structured Method and Unstructured Method," AIAA Paper 2004-0398, Jan. 2004.

[13]Shima, E., "A Simple Implicit Scheme for Structured/Unstructured CFD," *Proceedings of 29th Fluid Dynamics Symposium*, 1997, pp. 325–328 (in Japanese).

[14]Nakahashi, K., Togashi, F., Fujita, T., and Ito, Y., "Numerical Simulations on Separation of Scaled Supersonic Experimental Airplane from Rocket Booster at Supersonic Speed," AIAA Paper 2002-2843, June 2002.

[15]Ito, Y., and Nakahashi, K., "Direct Surface Triangulation Using Stereolithography Data," *AIAA Journal*, Vol. 40, No. 3, 2002, pp. 490–496.

[16]Ito, Y., and Nakahashi, K., "Surface Triangulation for Polygonal Models Based on CAD Data," *International Journal for Numerical Methods in Fluids*, Vol. 39, No. 1, 2002, pp. 75–96.

[17]Sharov, D., and Nakahashi, K., "A Boundary Recovery Algorithm for Delaunay Tetrahedral Meshing," *Proceedings of 5th International Conference on Numerical Grid Generation in Computational Field Simulations*, 1996, pp. 229–238.

[18]Ito, Y., and Nakahashi, K., "Improvements in the Reliability and Quality of Unstructured Hybrid Mesh Generation," *International Journal for Numerical Methods in Fluids*, Vol. 45, No. 1, 2004, pp. 79–108.

[19]Obayashi, S., and Guruswamy, G. P., "Convergence Acceleration of an Aeroelastic Navier–Stokes Solver," *AIAA Journal*, Vol. 33, No. 6, 1995, pp. 1134–1141.

[20]Sharov, D., and Nakahashi, K., "Reordering of Hybrid Unstructured Grids for Lower-Upper Symmetric Gauss-Seidel Computations," *AIAA Journal*, Vol. 36, No. 3, 1998, pp. 484–486.

[21]Spalart, P. R., and Allmaras, S. R., "A One-Equation Turbulence Model for Aerodynamic Flows," *La Recherche Aerospatiale*, No. 1, 1994, pp. 5–21.

[22]Matsuo, Y., Nakamura, T., Tsuchiya, M., Ishizuka, T., Fujita, N., Ohkawa, H., Hirabayashi, Y., Takaki, R., Yoshida, M., Nakamura, K., Yamamoto, K., Suematsu, K., and Iwamiya, T., "Numerical Simulator III—Building a Terascale Distributed Parallel Computing Environment for Aerospace Science and Engineering," *Proceedings of the Parallel CFD 2002 Conference*, Elsevier Science B. V., 2003, pp. 187–194.

[23]Haase, W., Chaput, E., Elsholz, E., Leschziner, M. A., and Müller, U. R., "ECARP—European Computational Aerodynamics Research Project: Validation of CFD Codes and Assessment of Turbulence Models," *Notes on Numerical Fluid Mechanics*, Vol. 58, 1997.

[24]Lei, Z., Murayama, M., Takenaka, K., and Yamamoto, K., "CFD Validation for High Lift Devices: Two-Element Airfoil," *Proceedings of 2004 KSAS-JSASS Joint Symposium on Aerospace Engineering*, 2004, pp. 200–206.

[25]Roache, P. J., "Perspective: A Method for Uniform Reporting of Grid Refinement Studies," *Journal of Fluids Engineering*, Vol. 116, Sept. 1994, pp. 405–413.

[26]Sharov, D., and Fujii, K., "Three-Dimensional Adaptive Bisection of Unstructured Grids for Transient Compressible Flow Computations," AIAA Paper 95-1708, June 1995.

[27]Moir, I. R. M., "Measurements on a Two-Dimensional Aerofoil with High-Lift Devices," AGARD Advisory Rept. 303: *A Selection of Experimental Test Cases for the Validation of CFD Codes*, Vols. 1 and 2, 1994.

[28]Fejtek, I., "Summary of Code Validation Results for a Multiple Element Airfoil Test Case," AIAA Paper 97-1932, June 1997.

[29]Johnson, P., Jones, K. M., and Madson, M., "Experimental Investigation of a Simplified 3D High Lift Configuration in Support of CFD Validation," AIAA Paper 2000-4217, Aug. 2000.